



Synthetic routes, structure and catalytic activity of Ag/BN nanoparticle hybrids toward CO oxidation reaction

Anton S. Konopatsky^{a,*}, Denis V. Leybo^a, Konstantin L. Firestein^c, Zakhar I. Popov^a, Andrey V. Bondarev^a, Anton M. Manakhov^a, Elizaveta S. Permyakova^a, Dmitry V. Shtansky^a, Dmitri V. Golberg^{b,c}

^a National University of Science and Technology "MISIS", Leninsky Prospekt 4, Moscow 119049, Russian Federation

^b World Premier International Center for Materials Nanoarchitectonics (WPI-MANA), National Institute for Materials Science (NIMS), Tsukuba, Namiki 1, Ibaraki 3050044, Japan

^c Science and Engineering Faculty, Queensland University of Technology, 2nd George st., Brisbane, QLD 4000, Australia

ARTICLE INFO

Article history:

Received 26 July 2018

Revised 8 October 2018

Accepted 10 October 2018

Available online 24 October 2018

Keywords:

Ag/BN nanohybrids

Catalytic activity

CO oxidation

Structural characterization

DFT calculation

ABSTRACT

Nanohybrid materials made of *h*-BN nanoparticles (BNNPs) with Ag nanoparticles (AgNPs), covering their surfaces, were employed as catalysts in CO oxidation reaction. Ag/BN nanohybrids (NHs) were produced via AgNO₃ decomposition under UV irradiation in polyethylene glycol (PEG) and its solutions at room temperature. Influence of the synthetic media composition on the synthesis process and resultant NHs structures were investigated. Two different structural types (Ag/BN and polymer-based structure) formed during the synthesis were studied. It was demonstrated that Ag/BN NHs synthesized in a PEG media had possessed the highest Ag concentration and uniform distribution of AgNPs. Catalytic activity tests revealed that the lowest temperature of full CO conversion (194 °C) had been attained to the sample with the highest Ag content. CO oxidation mechanism on the surface of AgNPs was finally proposed based on DFT calculations.

© 2018 Elsevier Inc. All rights reserved.

1. Introduction

Hexagonal boron nitride (*h*-BN) has been proved to be versatile and prospective material for various applications because of its outstanding mechanical properties, high chemical inertness and thermal stability [1–8]. Lately it has drawn a worldwide attention as a prospective nanohybrid material once having catalytically-active elements on its surface. Many studies were dedicated to the investigation of *h*-BN surface features and selection of catalytic surface-decorating materials, as well as to the nanohybrid production methods and their performance in catalytic and related processes [9–17].

Catalytic activity of Ag nanoparticles (AgNPs) was under the spotlight for many years. Special attention was paid to adjusting different AgNPs production methods in order to obtain preferable particle shape and structure [18–28]. It was shown that polyol method offers a promising route for a control over AgNPs structure through variation of AgNO₃/polyol ratio [29–31]. Earlier works dedicated to the investigation of polyols' role in AgNPs formation mechanism not only revealed a stabilizing

effect of different polyols, such as polyvinylpyrrolidone (PVP) and polyethyleneglycol (PEG) of different molecular weight, but also demonstrated their significance in silver nitrate reduction [32,33]. Advances of polyol method impel fabrication of more interesting nanocomposites and nanohybrid materials for catalytic purposes [21,29,34,35].

Along with global industrial development, materials science faces new challenges. Hence there is a high demand for new catalytic materials for carbon monoxide oxidation. While classic and well-known catalysts for CO oxidation were thoroughly studied and many promising results were obtained [36–39], the development of new materials is still a top-priority task. Selection of right carriers and catalytically active elements is the defining step on a way toward obtaining novel catalysts with enhanced functional properties. The prospects of *h*-BN as a carrier for noble metals, such as Pt and Au, that could be effectively used in CO oxidation reaction, have already been confirmed [40,41]. On the other hand, utilization of much more economically efficient elements, such as Ag, on BN surfaces has received less attention [42–45]. Despite of theoretical studies that predicted attractive functional properties of Ag/BN catalysts for CO oxidation [46,47], very few experimental studies were conducted. For example, one research dedicated to CO oxidation confirmed a catalytic effect of porous *h*-BN micro-meshes with AgNPs deposited on their surfaces (although at a

* Corresponding author at: National University of Science and Technology "MISIS", Leninsky Prospekt 4, Moscow, Russian Federation.

E-mail addresses: konopatskiy@misys.ru (A.S. Konopatsky), shtansky@mail.ru (D.V. Shtansky), dmitry.golberg@qut.edu.au (D.V. Golberg).

rather high temperature and with less than 100% CO conversion) [48].

Here we focus on the processes and structures in relation to the synthesis of Ag/BN nanohybrids (NHs) in polyol solutions, as well as on their catalytic performance in CO oxidation reaction. To the best of our knowledge, this is the first comprehensive study of nanoscale Ag/h-BN system in terms of its application for CO oxidation. Particular attention was paid to the study of the role of synthetic media composition on the integral Ag content and Ag distribution over *h*-BN support surface.

2. Experimental

2.1. Samples preparation

h-BN nanoparticles (BNNPs) produced by a plasma method (Plasmaterm, Russia) were used as carriers for AgNPs. The size of individual BNNPs was in the range of 20–80 nm. In order to obtain a moderate amount of boron oxide on the nanoparticle surfaces, the BNNPs were subjected to high temperature (1500 °C) vacuum annealing followed by short time oxidative annealing at 1100 °C in air. More detailed information on the heat treatment scheme was given elsewhere [43].

An ultrasonic homogenizer and a magnetic mixer were used to disperse BNNPs in the synthesis media. Low molecular polyol polyethylene glycol-400 (PEG) and isopropyl alcohol (IPA) at different ratios were used as the media. An AgNO₃ powder was added to the BNNPs/PEG/IPA mixture. Chemical decomposition of AgNO₃ at room temperature under ultraviolet (UV) irradiation (wavelength $\lambda = 185$ nm) was used for Ag/BN NHs production. Two groups of samples were prepared. The first group included samples that were subjected to single rinsing in IPA after synthesis. The obtained in such manner samples were marked as BN/Ag_s with the corresponding numbers (Table 1). These samples were used to investigate different types of structures that had been formed during the Ag/BN synthesis, since single rinsing in IPA allows us to preserve materials structure mostly intact. Samples of the second group were obtained through a three-time precipitation rinsing in distilled water and marked as BN/Ag with the corresponding numbers (Table 1). These samples were used as final Ag/BN catalysts without any byproducts that could appear during the syntheses.

Table 1
Samples description.

Group	Sample	Preparation features
1	Ag/BN_1s	Media (PEG-400 50 ml); single rinsing in IPA
	Ag/BN_2s	Media (PEG-400 5 ml + IPA 45 ml); single rinsing in IPA
	Ag/BN_3s	Media (PEG-400 1 ml + IPA 49 ml); single rinsing in IPA
	Ag/BN_4s	Media (IPA 50 ml); single rinsing in IPA
2	Ag/BN 1	Media (PEG-400 50 ml); triple rinsing in distilled water
	Ag/BN 2	Media (PEG-400 5 ml + IPA 45 ml); triple rinsing in distilled water
	Ag/BN 3	Media (PEG-400 1 ml + IPA 49 ml); triple rinsing in distilled water
	Ag/BN 4	Media (IPA 50 ml); triple rinsing in distilled water

2.2. Chemical and structural analysis

Chemical composition of Ag/BN NHs was investigated through scanning electron microscopy (SEM) and energy-dispersive spectroscopy (EDS) on a JSM 7600F instrument (JEOL) equipped with an EDS X-ray detector, and inductively coupled plasma mass spectrometry (ICP-MS) using a iCAP Q device (Thermo Scientific). Sample microstructures were evaluated by transmission electron microscopy (TEM), high-resolution TEM (HR-TEM), scanning TEM (STEM) and high-angular dark field STEM (HADF-STEM) on a 200 kV JEM-2100 instrument. Chemical surface states were investigated by Fourier-transform infrared spectroscopy (FTIR) using a Vertex 70v (Bruker). Chemical bonding on the sample surfaces was analyzed by X-ray photoelectron spectroscopy (XPS) using an Axis Supra spectrometer (Kratos Analytical). The maximum lateral dimension of the analyzed area was 0.7 mm. The spectra were fitted using CasaXPS software after subtracting Shirley-type background. The full width at a half maximum (FWHM) of boron and nitrogen peaks was set to 1.3 ± 1 eV and 1.5 ± 0.2 eV, respectively.

2.3. Catalytic tests

Catalytic performance of Ag/BN NHs was analyzed using carbon monoxide (CO) oxidation in a fixed-bed continuous-flow reactor at ambient pressure. In a typical experiment, 60 mg of the catalyst, diluted with quartz granules, was placed in an U-tube. Prior to analysis, the catalyst was activated in a flow of 20% O₂/80% He at 400 and 500 °C followed by reduction in 20% CO/80% He or 20% H₂/80% He at 250 or 200 °C, respectively, with a total flow rate of 25 ml/min. The activity measurements were done with 4% CO, 16% O₂ and 80% He gas flow under a total flow rate of 25 ml/min (GHSV = 25,000 ml·g_{cat}⁻¹·h⁻¹). Reaction products were analyzed by a mass-spectrometer (Thermostar). The conversion of CO gas was calculated using the equation:

$$X = 1 - \frac{f_{CO}^f}{f_{CO}^i}$$

where f_{CO}^f – CO gas flow rate after the catalyst bed; f_{CO}^i – initial CO gas flow rate.

2.4. Modeling

Quantum-chemical modeling was performed within the framework of Density Functional Theory (DFT) [49,50] using plane-wave basis set and the PAW method [51,52] as implemented in VASP [53–55]. Generalized gradient approximation (GGA) was used in the form of PBE (Perdew-Burke-Ernzerhof) exchange-correlation functional [56]. For exploring transition states and potential energy barrier calculations, the nudged elastic band method (NEB) [57] was used. For the Brillouin zone sampling gamma-centered Monkhorst-Pack scheme [58] with a $2 \times 2 \times 1$, k-point mesh was chosen. The plane wave basis cut-off energy $E_{\text{cutoff}} = 400$ eV was used. Grimme DFT-D3 corrections [59] were applied to include van der Waals interactions into the consideration. While the periodic boundary conditions are necessarily to be applied to simulation cells in the plane wave basis, one has to separate the metal slab from the periodic images in the neighboring cells in order to model an isolated surface. For this purpose, a vacuum spacing of 20 Å, perpendicularly to the metal plane, was set in the simulation cell. In all geometry optimizations, the convergence criterion was so that the maximal force acting on any atom was less than 0.01 eV/Å. All structures were visualized in VESTA [60].

3. Results

3.1. Microstructure of Ag/BN nanohybrids

3.1.1. SEM analysis

The relationship between structures and chemical states of Ag/BN_s samples was investigated by SEM and FTIR methods. After the synthesis, an obtained mixture was centrifuged and the precipitated product was collected for another rinsing in IPA. Procured materials (Ag/BN_s) were dried and their structures were investigated by SEM. Fig. 1 depicts a typical structure of Ag/BN_s samples obtained at different conditions (Table 1). According to the obtained SEM images, Ag/BN_s samples were represented by Ag/BN NHs agglomerates and some ribbon-like flakes. The length of ribbons significantly varied. The largest amount of ribbons can be seen in case of Ag/BN₁s NHs obtained in a media consisted of PEG only (Fig. 1a). Some ribbon-like structures can be also seen in case of Ag/BN₂s NHs (Fig. 1b). Note that Ag/BN₃s and Ag/BN₄s samples were completely free of such structures (Fig. 1c,d). So, the amount of ribbon-like structures decreased as the concentration of PEG in the synthesis media decreased.

3.1.2. FTIR spectroscopy

FTIR spectra obtained for Ag/BN_s samples are given in Fig. 2. Characteristic BN peaks are well seen at corresponding wave numbers (maxima at 820 and 1400 cm⁻¹). The FTIR spectrum of Ag/BN₁s sample reveals a strong additional peak at 1089 cm⁻¹ and weaker peaks at 1350, 1250, 940 and 680 cm⁻¹ that could be assigned to C–O–C, C–H, O–H, C=C, C=C bonds of PEG [21,61–63]. A similar FTIR spectrum was observed for Ag/BN₂s sample but the corresponding peaks are less pronounced. Only traces of the regarded peaks can be seen in case of Ag/BN₃s NHs.

3.1.3. High-resolution TEM analysis

TEM and STEM images of the Ag/BN NHs are presented in Fig. 3. It can be seen that the AgNPs in Ag/BN 1 sample are rather small,

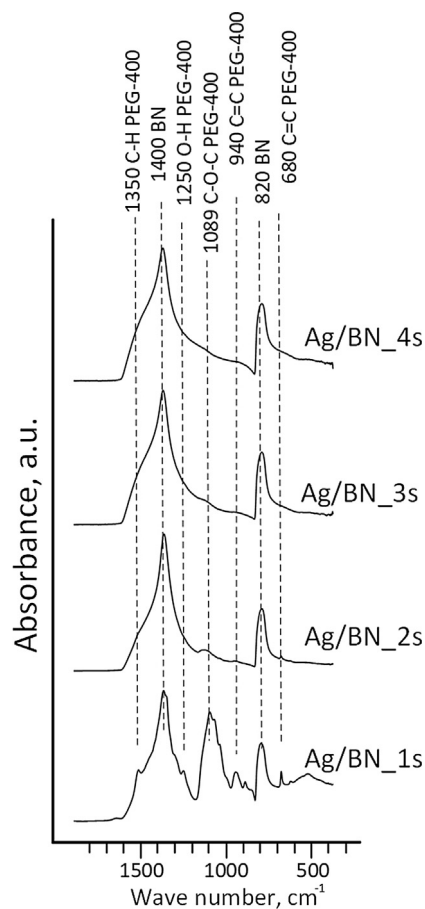


Fig. 2. FTIR spectra of Ag/BN_s samples.

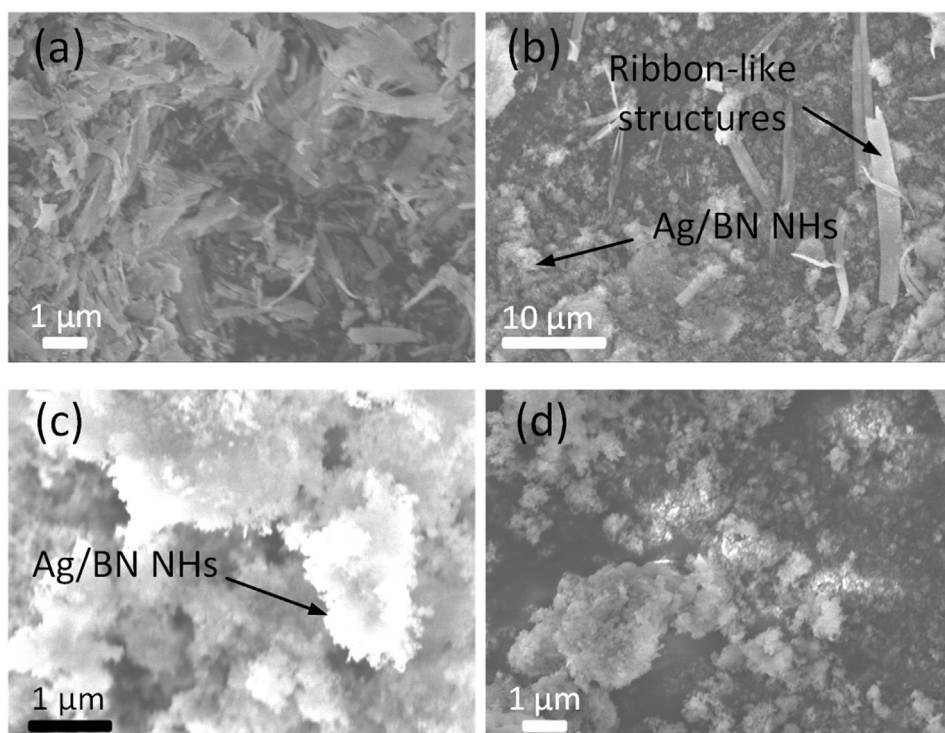


Fig. 1. Typical structure of Ag/BN_s samples as revealed by SEM: (a) Ag/BN₁s, (b) Ag/BN₂s, (c) Ag/BN₃s, (d) Ag/BN₄s.

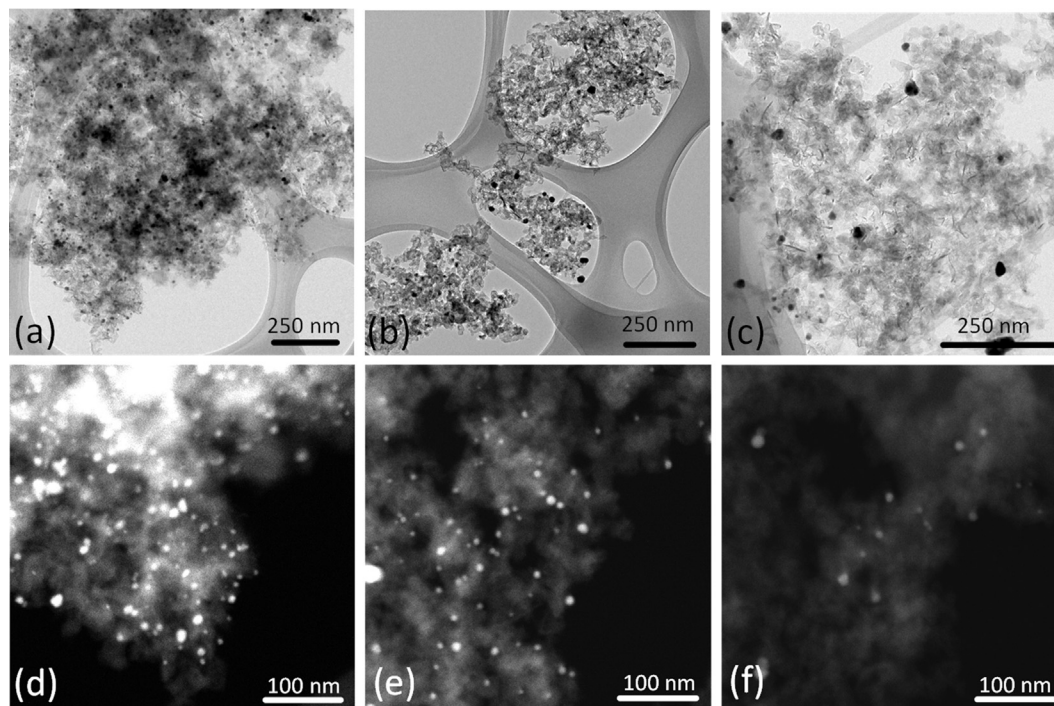


Fig. 3. TEM (a–c) and STEM (d–f) micrographs of Ag/BN NHs: (a) – Ag/BN 1, (b) – Ag/BN 3; (c) – Ag/BN 4, (d) – Ag/BN 1, (e) Ag/BN 3; (f) Ag/BN 4.

5–10 nm in average size, and densely populate the BN support surface. TEM data also allowed us to conclude that the uniformity of AgNPs distribution, as well as their density over BN surfaces, decreases in case of other samples Ag/BN 2, Ag/BN 3 (Fig. 3b,e) and Ag/BN 4 (Fig. 3c,f), i.e. BNPs without any AgNPs on their surfaces can be frequently seen. Note that the structure of Ag/BN 2 sample was similar to that of Ag/BN 3 and, therefore, not shown here. However, if AgNPs are visible, their sizes are in general similar to those in the Ag/BN 1 sample.

Fig. 4 depicts the HADF-STEM image and the corresponding EDS maps for Ag/BN 1 sample. Ag and O element distributions (Fig. 4c) indicate that spherical NPs (of bright contrast) observed in the TEM image (Fig. 4a) are indeed AgNPs that do not contain significant amount of oxygen. Fig. 4b demonstrates the HR-TEM image of an individual AgNP. Fast Fourier transform (FFT) pattern (Fig. 4b inset) allowed us to measure Ag interplanar distances as follows: $d_1 = 0.235$ nm, $d_2 = 0.207$ nm, $d_3 = 0.141$ nm and $d_4 = 0.122$ nm. These could be assigned to a face-centered cubic silver with

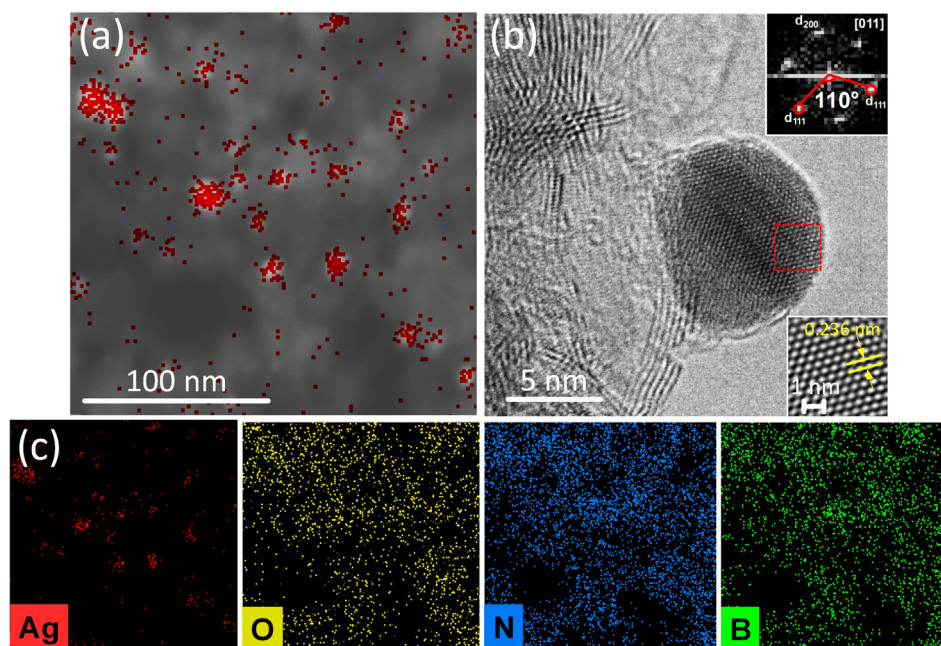


Fig. 4. HADF-STEM (a) and HR-TEM (b) images of the Ag/BN 1 sample with corresponding spatially-resolved Ag, B, N and O EDS maps (c) of AgNPs shown in panel (a). Insets in (b) demonstrate FFT pattern and FFT filtered image obtained from the framed area.

Table 2
Ag content in Ag/BN NHs.

Sample	Ag/BN 1	Ag/BN 2	Ag/BN 3	Ag/BN 4
Ag, wt.%	1.36 ± 0.3	0.77 ± 0.01	0.83 ± 0.03	0.63 ± 0.01

$d_{(111)} = 0.236$ nm, $d_{(200)} = 0.204$ nm, $d_{(220)} = 0.144$ nm and $d_{(311)} = 0.123$ nm, respectively. It can be also seen that the angle between the marked (1 1 1) crystallographic planes in the FFT image is 110°, which further confirms the *fcc* structure of the present AgNPs.

Integral concentration of AgNPs determined by ICP-MS method was used as a decent characteristic during NHs comparison. The results are given in Table 2. It can be seen that Ag/BN 1 sample synthesized in PEG contains more than twice as much Ag as compared to Ag/BN 4 NHs synthesized in IPA, while Ag content in Ag/BN 2 and 3 NHs was intermediate between samples 1 and 4.

3.1.4. XPS analysis

XPS Ag3d spectra of the Ag/BN NHs are depicted in Fig. 5a. Due to a low concentration of silver, the noise to signal ratio was rather low, which complicates the spectra interpretation. Nevertheless the binding energy of Ag 3d 5/2 peak of each sample corresponds to a metallic silver.

B 1s and N 1s spectra of Ag/BN 1, 2 and 3 samples were similar, whereas those of Ag/BN 4 NHs revealed slight differences (Fig. 5b, c). The XPS B 1s spectra of all samples were deconvoluted into two components. The most intensive B 1s component at 190.6 eV was assigned to the atomic environment of B atom having only nitrogen atoms, similar to the structure of pure *h*-BN. The second component, NBO at 191.9 eV, corresponds to the B atoms having chemical bonds with oxygen and nitrogen. The single maximum observed in the XPS N 1s spectra of Ag/BN 1, 2 and 3 samples can be well divided into two main components positioned at 398.3 and 398.8 eV; these are also attributed to the BN and NBO phases. The fitting of XPS N 1s spectrum of sample 4 required the addition of third NH⁺ peak centered at 400.0 eV. The contents of all elements, as well as B and N environments, are summarized

in Tables 3 and 4. The Ag content (Table 4) was in a good agreement with the ICP-MS data.

3.2. Catalytic performance

Catalytic activity of the Ag/BN NHs was studied up to the temperature of 100% CO conversion. The tests were conducted for samples with and without preliminary activation stage in order to evaluate its influence on catalytic performance. Different activation schemes were implemented: (i) heating up to 500 °C (30 min) in oxygen and then reduction in CO at 250 °C (30 min), (ii) heating in oxygen up to 400 °C (30 min), and (iii) heating in oxygen up to 400 °C with following reduction in H₂ at 200 °C (30 min). The obtained results are presented in Fig. 6.

The best catalytic activity can be seen in case of the Ag/BN 1 sample without any activation followed by Ag/BN 2, 3 and 4 in order of their numbering (Fig. 6a). It is also worth noting that the growth rate of catalytic activity is rather high and the temperature range for the full CO conversion is narrow. As for samples activated

Table 3
Concentrations of different boron and nitrogen environments in Ag/BN NHs.

Sample	Concentration, at.%				
	B–N	N–B–O	B–N	N–B–O	N–H ⁺
Ag/BN 1	75.0	25.0	63.3	36.7	0.0
Ag/BN 2	81.1	18.9	62.7	37.3	0.0
Ag/BN 3	78.7	21.3	69.0	31.0	0.0
Ag/BN 4	86.1	13.9	65.1	30.2	4.7

Table 4
Contents of elements in Ag/BN NHs.

Sample	Content, at.%			B/N
	Ag	B	N	
Ag/BN 1	0.16	39.7	43.0	0.92
Ag/BN 2	0.10	42.4	48.2	0.88
Ag/BN 3	0.11	42.5	47.8	0.89
Ag/BN 4	0.07	42.7	47.8	0.89

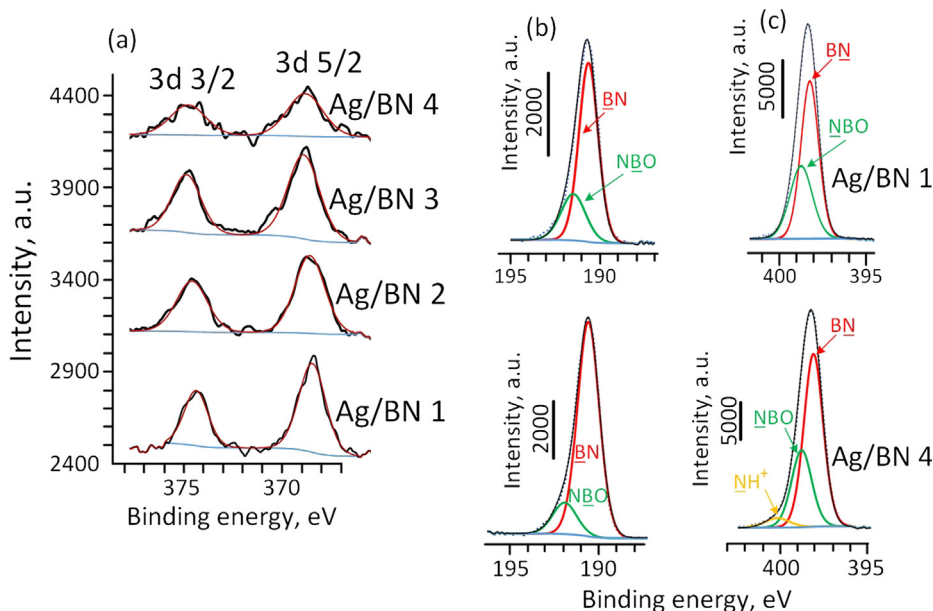


Fig. 5. XPS Ag3d (a), B1s (b) and N1s (c) spectra of Ag/BN NHs.

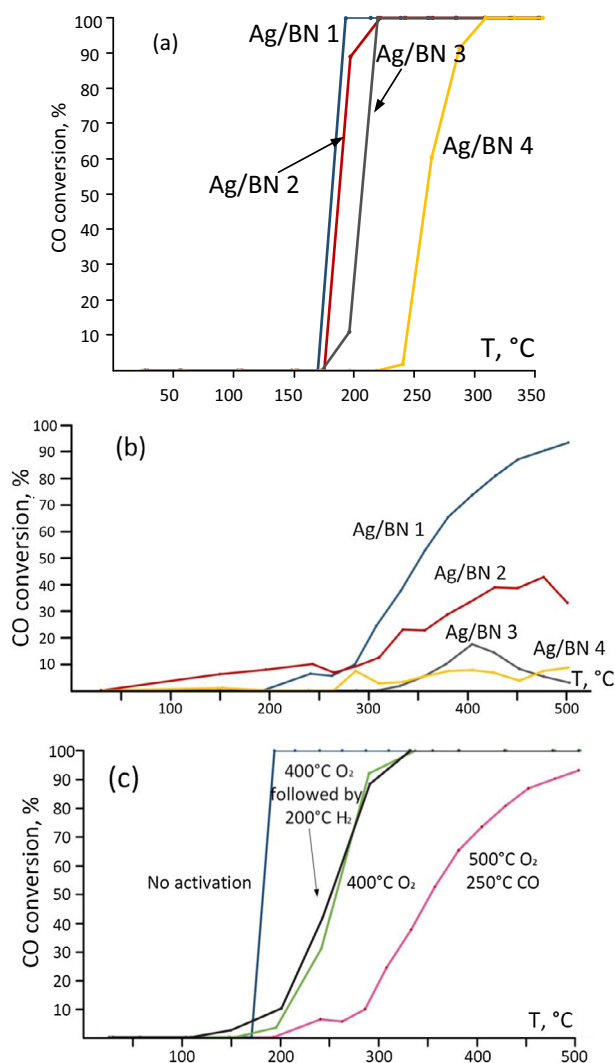


Fig. 6. Catalytic activity of Ag/BN NHs: (a) – no activation; (b) – activation at 500 °C; (c) different activation routes for Ag/BN 1 NHs.

in oxygen at 500 °C (with a consequent reduction in CO at 250 °C), they demonstrate a rather poor catalytic performance with gradually decreasing activity as PEG concentration decreases in the synthesis media (Fig. 6b). Only Ag/BN 1 sample demonstrates close to 100% CO conversion, but at a fairly high temperature, while all other samples did not show better than 40% conversion, at best. In the last case, the temperature range, in which reaction takes place, is quite wide. Fig. 6c illustrates the influence of different schemes of activation on Ag/BN 1 catalytic activity. It can be seen that oxidation at lower temperatures increased catalytic activity. This probably indicates more promising activation routes at the lower temperature ranges. Interestingly, catalytic activity obtained after oxidation at 400 °C in O₂ is almost identical to that obtained after the same oxidation and followed by reduction in H₂ at 200 °C.

4. Discussion

4.1. Scheme of Ag/BN NHs synthesis

As follows from Figs. 1 and 2, the Ag/BN_1s sample containing a great amount of ribbons also demonstrates the presence of chemical bonds originated from PEG-400. The same correlation holds for Ag/BN_2s NHs, but in this case, a smaller amount of ribbons and

correspondingly weaker FTIR signal from PEG-400 are apparent. Such pattern allows us to conclude that this ribbon-like structure has a polymer (PEG-400) basis. Additionally it is worth to mention that these structures are easily dissolved in distilled water which further supports a suggestion of their polymer-based origin. The SEM images presented in Fig. 7 allow us to conduct a closer inspection of the ribbon-like structure. Since the observed structure is polymer-based, even a mild thermal treatment should lead to its degradation. Thus the ribbons' heat treatment was conducted in a desiccator filled with air at 100 °C for 4.5 h. Fig. 7a shows that ribbons have a width of up to 2 μm and a thickness of up to 100 nm, while their length often exceeds 10 μm. As it can be seen from Fig. 7b, after mild heat treatment numerous spherical nanoparticles become visible on the ribbon surfaces. In order to investigate the chemical composition of such structure EDX analysis was conducted. Fig. 7c,d depicts SEM image and corresponding elemental map of Ag. The results of EDX analysis demonstrate that high concentration of Ag is peculiar to these ribbons. Elemental map for Ag precisely repeats the ribbons arrangement on the corresponding SEM image. Thus the spherical particles are in fact Ag-based inclusions.

The following mechanism could be proposed to describe ribbon-like structure formation. Different polyols (in our case PEG-400) have already been successfully used to stabilize Ag and other catalytically active elements via the polyol process. At certain conditions such materials may form a metallogel. Its form heavily depends on the synthesis conditions and is often represented by entangled fiber tapes and other structures consisting of AgNPs and a matrix whose composition depends on the synthesis media [64,65]. Combined decomposing effect of UV and PEG on AgNO₃ and the following reduction of released Ag ions ultimately result in metallic Ag clusters and nanoparticles formation. The following processes involving those AgNPs could be outlined. In the first instance AgNPs and BNPs collision led to Ag/BN NHs formation. Secondly, AgNPs became isolated by PEG macromolecules. Then those structures built up into large-scale ribbons with a polyol matrix. The proposed scheme is given in Fig. 8. In our case, extensive amount of PEG and a relatively high concentration of AgNO₃ procure conditions needed for metallogel formation with such ribbon-like structure (Ag/BN 1 and 2). Decreasing concentration of PEG to a certain point results in a deficiency of macromolecules needed for the metallogel formation (Ag/BN 3). Taking such scenario into account it can be concluded that two competitive processes take place during the synthesis with considerable amount of PEG in the media: (i) formation of Ag metallogel; and (ii) formation of Ag/BN NHs. A large amount of AgNPs recovered from nitrate is involved in the metallogel formation, which becomes a byproduct of Ag/BN NHs.

4.2. Influence of media composition on the synthetic process and Ag/BN NHs structure

Statistical analysis of TEM images was conducted in order to evaluate AgNPs sizes distribution. Samples were rearranged in 3 groups according to the synthesis media: PEG, PEG-IPA solution and IPA. The obtained results are given in Fig. 9.

In order to interpret the obtained histograms we should first take into account some key aspects. Not less than 15 different agglomerates of Ag/BN NHs were investigated by TEM for each sample. And while almost all agglomerates of AgBN 1 sample contained a considerable amount of uniformly distributed AgNPs, other samples demonstrated somewhat different picture. Overall, AgNPs density was lower and BNPs agglomerates with only a few or none AgNPs were more common in AgBN 4. The same, but less pronounced feature holds for the structure of AgBN 2 and 3 with no noticeable differences between the two. These

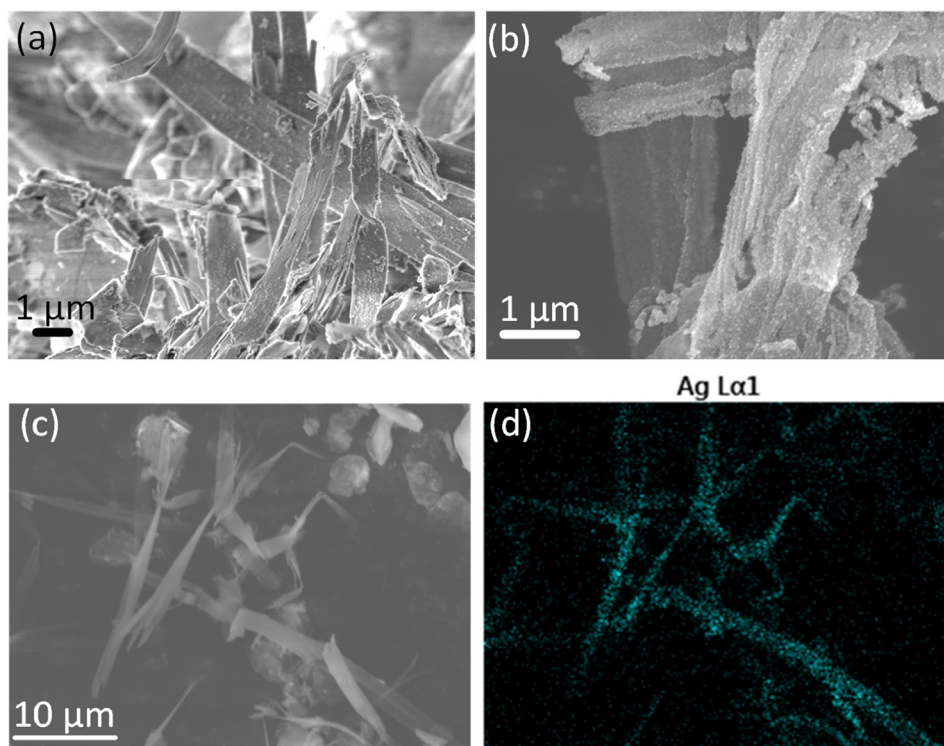


Fig. 7. SEM images of a ribbon-like structure (a–c) with corresponding elemental map of Ag (d). (a,c) as-produced structure, (b) after annealing in air at 100 °C for 4.5 h.

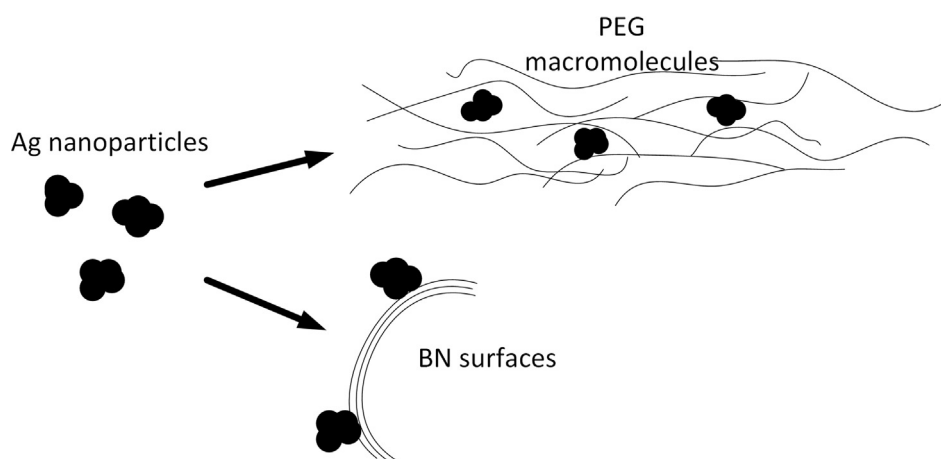


Fig. 8. Scheme of Ag/BN NHs synthesis.

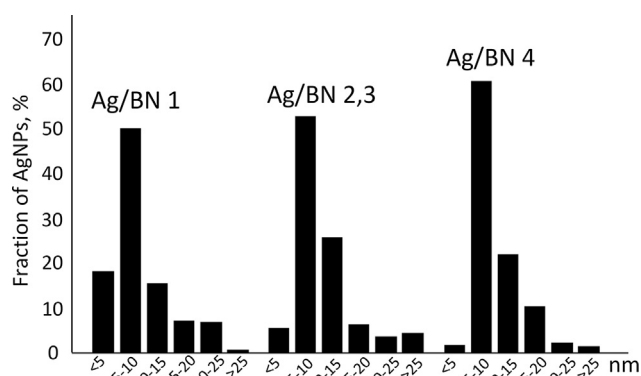


Fig. 9. AgNP sizes distribution.

aspects correspond well with ICP-MS data (Table 2). Indeed, Ag/BN 1 sample with a high amount of AgNPs on its surface (Fig. 3a,b) demonstrates the highest Ag concentration (Table 2). The same tendency is observed for other samples as the AgNPs density gets lower, uniformity of their distribution also decreases and Ag content becomes correspondingly lower. It follows from Fig. 9 (Ag/BN 1) that the size of majority of AgNPs is under 10 nm, when PEG is the sole component of the synthesis media. It is clear that AgNPs distribution shifts towards larger particles in case of Ag/BN 2 and 3 samples produced in the PEG-IPA solution. The size of larger particles reaches 55 nm. The larger amount of “empty” BN agglomerates can be found in case of Ag/BN 4 sample. And Ag/BN NHs that still had AgNPs demonstrate similar to Ag/BN 2 and 3 sizes distribution (5–10 nm). PEG plays the two main roles in NHs synthesis: it acts as both stabilizing and reducing agent. It

stabilizes not only reduced AgNPs, thus preventing their growth, but also their BNNPs carriers. Indeed, the precipitation process of dispersed BNNPs is inhibited in PEG and is significantly more accelerated in examined solutions and IPA. This leads to enclosure of some part of BNNPs' surfaces, which were potentially available for AgNPs deposition. By contrast, uniform distribution of not aggregated *h*-BN in the synthesis media led to a greater amount of surfaces potentially suitable for AgNPs deposition. For this reason, it could be suggested that there is a dependence of the number of the BN surfaces available for AgNPs deposition on the PEG content in the synthesis media. This means that the media that effectively prevents particles aggregation should be more favorable in terms of obtaining higher concentration of catalytically active particles over carriers' surfaces. Appearance of AgNPs of larger sizes could be also assigned to a decrease of PEG content and, hence, a lower aggregative stability of the synthesis media in case of Ag/BN 2 and 3 samples. As for reducing effect of PEG, it also plays a significant role, since the smaller fraction of initial AgNO₃ is decomposed. This leads to a lower net content of AgNPs in reaction volume. This has its own contribution to the lower AgNPs density over BN surfaces. It is also suggested that PEG's performance as a reductant decreases slower compared to its stabilizing effect, as PEG's content decreases in the synthesis media. A narrow size distribution and an overall small size of AgNPs in Ag/BN 4 sample are explained as follows. In the absence of PEG UV irradiation is left as the only driving force of AgNO₃ reduction, setting a slower pace of such reaction compared to the synthesis in other studied media. In such manner deterred formation of AgNPs limits the time accessible for the particle growth explaining their smaller size. Combination of those factors (decreasing in stabilizing and reducing effects of the media with a smaller content of PEG) explains a greater number of "empty" BN agglomerates.

According to Fig. 5a, the Ag3d spectra could be fitted using a single curve. The peak positions indicate the presence of metallic silver over the BN surfaces being in a good agreement with TEM data (Fig. 4). XPS Ag3d peak positions are given in Table 5. The observed shift of the Ag3d 5/2 peaks (Fig. 5a) could be related to the different size of AgNPs in Ag/BN 1–4 samples (Fig. 9). Smaller AgNPs tend to demonstrate lower binding energy due to reduced coordination of Ag atoms [66,67].

As for carriers, comparing Fig. 4c (elemental maps) and Fig. 5 (XPS data), it can be concluded that the presence of uniformly distributed oxygen could be related to the BNO component of *h*-BN and probably originates from an intermediate between *h*-BN and B₂O₃ which was formed during short-time oxidation annealing. Another worth mentioning feature is related to the additional component in N1s peak of Ag/BN 4 sample (Fig. 5c). Although the content of NH⁺ component was small (Table 3), it can be ascribed to nitrogen protonation in synthesis media with a higher pH. However, due to its small content, it can be concluded that the entire set of samples exhibits very similar boron and nitrogen environment.

4.3. Factors affecting catalytic performance

Temperature of 100% CO conversion, as well as the temperature range in which oxidation reaction takes place, are both considered as the main factors determining the catalysts performance. Table 6 summarizes the results of catalytic activity tests. Ag/BN samples without activation demonstrate the best catalytic activity reaching a full CO conversion at 194 °C in case of Ag/BN 1 NHs. Ag/BN 2 and 3 samples show quite similar results: temperature of full CO conversion (246–248 °C) and reaction temperature range (47.5 °C). Ag/BN 4 NHs exhibit a poorer performance, showing a higher value of T₁₀₀ (311 °C). The fact that the onset temperature of catalytic CO oxidation does not change among samples without activation sug-

Table 5

Positions of Ag 3d 5/2 XPS peaks.

Sample	Ag/BN 1	Ag/BN 2	Ag/BN 3	Ag/BN 4
Ag3d 5/2, eV	368.4	368.6	368.7	368.7

Table 6

Catalytic activity characteristics.

Sample	Catalysts activation scheme	
	None Reaction temperature range, °C	500 °C O ₂ , 250 °C CO Full CO conversion temperature T ₁₀₀ , °C
Ag/BN 1	23	194 >500 (T ₉₃ = 503 °C)
Ag/BN 2	47.5	248 >>500
Ag/BN 3	47.5	246 >>500
Ag/BN 4	92	311 >>500

gests that similar types of active sites participate in the reaction. The increase of conversion rate from Ag/BN 4 to Ag/BN 1 originates from the increase of the amount of those sites. The results obtained for Ag/BN samples without activation correspond well with the concept of NHs structure changes in dependence on synthesis media. Indeed, more uniform distribution of AgNPs and their higher density over carrier surfaces, which also means a larger amount of individual particles, would greatly benefit catalytic activity, as proved by the Ag/BN 1 NHs. In that case PEG appears to be a more favored media for the Ag/BN NHs synthesis regardless of the fact that a significant part of reduced Ag was consumed for the metallogel formation. On the other hand, the results obtained for samples synthesized in the PEG diluted solutions indicate that even small additions of a given stabilizer facilitate formation of more uniformly distributed AgNPs and, hence, improve the catalytic performance (e.g. compare the curves for Ag/BN 2, 3 and 4 samples in Fig. 6a).

Usually, the proper activation route allows for a significant improvement of catalytic performance of a material. The Ag/BN samples without any activation should be used as a reference sample in that case. It follows from Fig. 6b that the catalytic activity drastically decreased after the following scheme of activation: heating at 500 °C in oxygen and consequent heating at 250 °C in CO. It could be suggested that such decrease is connected to the specifics of carrier surfaces and activation scheme. *h*-BN is highly resistant to oxidation, up to at least 600 °C, but taking into account a considerable amount of AgNPs on the BN surfaces, it becomes an important task to investigate whether the regarded oxidation process may take place at lower temperatures i.e. 500 °C. For that, an additional FTIR analysis was conducted for the Ag/BN 1 sample subjected to oxidation at 500 °C with the same gas flow rate as during activation. Obtained absorbance and absorbance differential spectra are given in Fig. 10.

It clearly follows from Fig. 10 that even Ag/BN NHs with the greatest amount of AgNPs (Ag/BN 1) at the highest temperature used during the activation (500 °C), keep excellent oxidation stability and do not reveal the B₂O₃ and O–B–O bonds in the range of 540–720 cm⁻¹. For that reason it could be concluded that the difference in catalytic activity is not connected to the changes in carriers' chemical state. The manner of catalytic activity degradation when looking at samples with or without activation (500 °C O₂, 250 °C CO) is vividly seen in case of Ag/BN 1 NHs (Fig. 6c). The curve growth rate drops significantly. This leads to a much wider temperature range of the studied reaction, i.e. 23 °C vs 311 °C, for Ag/BN 1 NHs without and with activation, respectively. This difference could be related to a decrease in a number of active sites on the BNNPs surfaces. Other activation routes were tested for

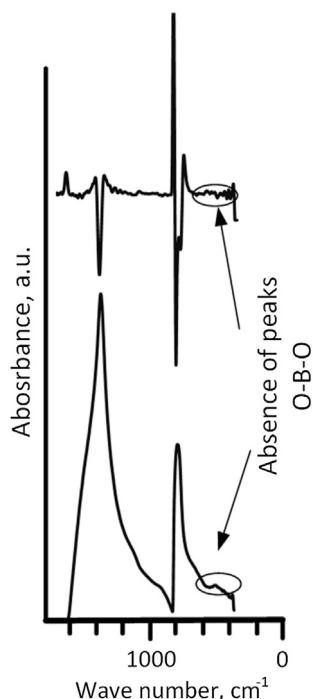


Fig. 10. FTIR spectra of Ag/BN 1 sample after oxidation at 500 °C for 30 min.

Ag/BN 1 sample. According to Fig. 6c, oxidation at a lower temperature (400 °C) leads to the improvements of catalytic activity (T_{100} is reached at 338 °C) compared to oxidation at a higher temperature (500 °C), but still the obtained results are notably worse than for the NHs without activation. It indicates that activation schemes, including oxidation at the lower temperatures, should have potential opportunities for a control over the catalytic activity of Ag/BN NHs toward CO oxidation reaction. It is worth to mention that the fact that catalyst reduction (200 °C in H_2), that had been implemented after oxidation, had almost no positive effect on catalytic activity ($T_{100} = 333$ °C). This also indicates that a proper selection of the optimal oxidation temperature plays a pivotal role in activation process.

In order to evaluate the AgNP size effect on the catalytic activity of the Ag/BN hybrids, additional experiments were carried out. Additional Ag/BN sample with larger Ag particle size (hereafter denoted as Ag/BN_L) was produced via ultraviolet (UV) decomposition of $AgNO_3$ in a mixture of polyethylene glycol and BNNPs as described elsewhere [43]. The results of catalytic activity study of Ag/BN_L sample are presented in Fig. 11. The TEM image shown in Fig. 11(inset) confirmed that the AgNP size significantly

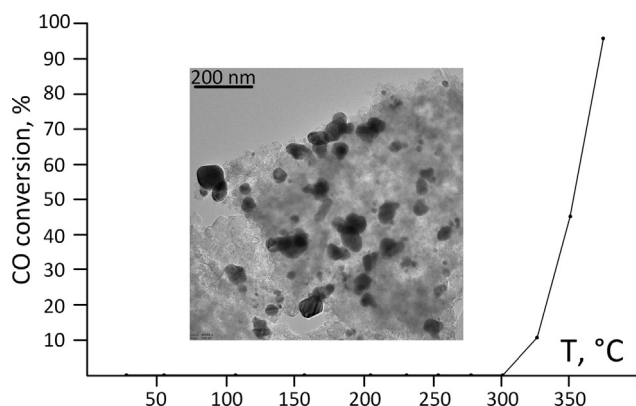


Fig. 11. Catalytic activity and TEM image (inset) of Ag/BN_L sample.

increased from 5 to 10 to 100 nm. Ag/BN_L sample reached nearly full CO conversion (94%) at 375 °C, which is significantly worse in comparison with BN/Ag_1 counterpart. Moreover, according to the ICP analysis, the Ag concentration in Ag/BN_L sample (4.63 ± 0.2 wt %) was more than three times higher than that in BN/Ag_1 NH. This indicates that the catalytic activity was more depended on specific surface area of catalytically active element than on its total content in the nanohybrid.

In further discussing the nanohybrid function it is worth noting that the AgNP content and their size distribution over the BNNP surface can be controlled by varying the surface chemical state of BN support. Optimal pretreatment of BNNPs allows one to effectively control Ag content on their surfaces and, therefore, to achieve higher catalytic performance of the Ag/BN NHs [43].

4.4. Mechanism of CO oxidation

CO oxidation mechanism on the surface of AgNPs was proposed based on DFT calculations. For this, the calculated sorption energies and oxygen dissociation barrier were calculated. This data is presented in Fig. 12 to reveal the possible reaction pathways. All calculations were performed on the $(111)_{Ag}$ surface. The choice of the $(111)_{Ag}$ surfaces for calculations is explained as follows: (i) experimental results indicated that the $(111)_{Ag}$ planes were roughly parallel to the $(0001)_{h-BN}$ planes (Ag NP presented in Fig. 4b is just a typical example showing this orientation) and (ii) the (111) planes of Ag NPs are low-energy planes, therefore, the Ag NPs are favored to form new surfaces with (111) crystallography [68]. Oxidation of a CO molecule involves overcoming two energy barriers associated with the dissociation of oxygen molecule and placing the CO molecule onto the sorption center, near the oxygen atom.

Initially, the different positions of adsorbed molecules were analyzed. The oxygen molecule was placed onto two different sorption sites, perpendicularly to the silver surface: on top of an Ag atom and between three Ag atoms. Location on top of Ag atom was energetically less favorable in comparison with the in plane position, 0.29 eV difference. Note that the distance between oxygen atoms for the adsorbed O_2 molecule was increased to 1.76 Å. This can be attributed to a partial filling of antibonding π -orbitals with Ag electrons. Despite the energy preference of such pre-dissociated state of the adsorbed oxygen molecule, our calculations using NEB showed that its further dissociation can only take place after overcoming the energy barrier of 0.82 eV.

Additionally, the diffusion barrier of the oxygen atom and CO molecule on the Ag surface was calculated, these were found to be 0.19 and 0.11 eV, respectively. Low diffusion barriers indicate a greater mobility of CO molecules and oxygen atoms on the Ag surface. So, we can consider the reaction of CO_2 formation as an additive reaction of an oxygen atom with a CO molecule in which they are placed at the neighboring sorption centers on the Ag surface. The formation of CO_2 molecules is energetically favorable

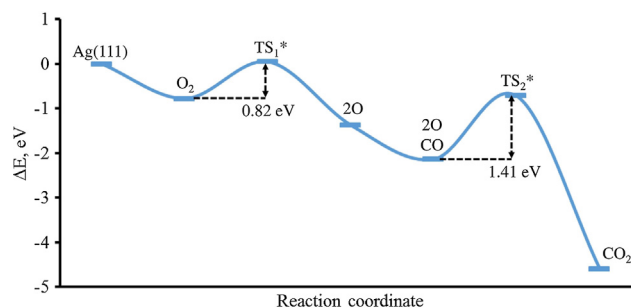


Fig. 12. Energy diagram for CO oxidation on an Ag surface.

Table 7

Results of our study compared to other reports.

Reference	T _{98–100} , °C	Catalyst	Ag, wt. %
This study	194	Ag/BN	1.36
[38]	65	Ag/SiO ₂	8
[48]	>500	Ag/BN micromesh	15
[36]	200	Ag-Co/Al ₂ O ₃	5
[26]	90	Ag/Carbon nanotubes	9.5

(Fig. 12), but requires overcoming a barrier of 1.42 eV for the CO molecule to move to the neighboring oxygen atom sorption center. This value is very close to the value of ~1.3 eV reported for a barrier of CO₂ molecule formation between adsorbed CO and O on the surface of Ru(0001) [69].

In contrast to the previously obtained results [70], where the mechanism of CO oxidation on Ag-Au nanoclusters was considered, in our case the dispersion interaction was taken into account, which complements the reaction map due to appearance of sorption energy of the oxygen molecule on the metal surface. This in turn contributes to an increase in the oxygen dissociation barrier on the Ag surface, as the adsorbed oxygen molecule is in the pre-dissociated state and the total energy of the system decreases.

Summarizing, we note that the oxidation of CO molecule involves overcoming two energy barriers associated with the dissociation of an oxygen molecule and placing a CO molecule onto the sorption center near the oxygen atom. We point out that in this work we have only considered the most obvious reaction pathway. In order to explore a very complex nature of the multi-dimensional potential energy surface in more detail, further calculations are required.

Table 7 compares the catalytic activity of the Ag/BN NHs and Ag contents in them with the data reported in the literature for other types of AgNPs supports. Note that the results presented in Refs. [26,38,54,55] were obtained for the catalysts with the optimized chemical compositions and carefully selected activation routes. The results clearly demonstrate that the present Ag/BN NHs are promising catalysts for CO oxidation having a great potential for further improvement of their catalytic characteristics by optimizing their chemical composition, synthesis media and activation scheme.

5. Conclusions

Ag/BN nanohybrid catalytic performance toward CO oxidation reaction was studied. It was demonstrated that the studied materials had a pronounced catalytic effect on the reaction rate. Two parallel processes, i.e. the formation of Ag/BN nanohybrids and Ag polymer-based metallogels, proceeded simultaneously when a certain content of PEG-400 was added into the synthesis media. The influence of PEG-400 content in the synthesis media on the integral Ag content, as well as uniform distribution of individual AgNPs over carriers' surfaces, were documented. The catalyst synthesized in the media with a sole PEG-400 component demonstrated the highest Ag content, uniform AgNPs distribution and the best catalytic activity with the temperature of full CO conversion of 194 °C. Preparatory studies of catalysts activation processes revealed possibilities of control over Ag/BN functional properties. DFT calculations indicated that the oxidation of CO molecule had involved overcoming two energy barriers associated with the dissociation of an oxygen molecule and placing a CO molecule onto the sorption center near the oxygen atom.

Acknowledgments

The authors gratefully acknowledge the financial support from the Ministry of Education and Science of the Russian Federation

(Increase Competitiveness Program of NUST “MISiS” No. K2-2017-082) in the part of catalytic activity tests and DFT calculations, and the Russian Foundation for Basic Research (Agreement 18-58-53034\18) in the part of Ag/BN NHs fabrication by reduction from a salt solution. D.G. is particularly grateful to the Australian Research Council (ARC) Laureate Fellowship FL160100089, and Queensland University of Technology (QUT) Project 322170-0355/51.

References

- [1] A. Pakdel, Y. Bando, D. Golberg, Nano boron nitride flatland, *Chem. Soc. Rev.* 43 (2014) 934–959.
- [2] X.F. Jiang, Q. Weng, X.-B. Wang, X. Li, J. Zhang, D. Golberg, Y. Bando, Recent progress on fabrications and applications of boron nitride nanomaterials: a review, *J. Mater. Sci. Technol.* 31 (2015) 589–598.
- [3] F.F. Xu, Y. Bando, D. Golberg, M. Hasegawa, M. Mitome, Phases and crystallization of encapsulated cobalt nanorods inside BN nanotubes, *Acta Mater.* 52 (2004) 601–606.
- [4] Y. Chen, J. Zou, S.J. Campbell, G. Le Caer, Boron nitride nanotubes: pronounced resistance to oxidation, *Appl. Phys. Lett.* 84 (2004) 2430–2432.
- [5] M.T. Sabatini, L.T. Boulton, T.D. Sheppard, Borate esters: simple catalysts for the sustainable synthesis of complex amides, *Sci. Adv.* 3 (2017) e1701028.
- [6] X. Li, X. Wu, Low-dimensional boron nitride nanomaterials, *J. Univ. Sci. Technol. China* 44 (2014) 389–440.
- [7] Q. Weng, X. Wang, X. Wang, Y. Bando, D. Golberg, Functionalized hexagonal boron nitride nanomaterials: emerging properties and applications, *Chem. Soc. Rev.* 45 (2016) 3989–4012.
- [8] Q. Weng, X. Wang, C. Zhi, Y. Bando, D. Golberg, Boron nitride porous microbelts for hydrogen storage, *ACS Nano* 7 (2013) 1558–1565.
- [9] D. Fan, J. Feng, J. Liu, T. Gao, Z. Ye, M. Chen, X. Lv, Hexagonal boron nitride nanosheets exfoliated by sodium hypochlorite ball mill and their potential application in catalysis, *Ceram. Int.* 42 (2016) 7155–7163.
- [10] G. Elumalai, H. Noguchi, H.C. Dinh, K. Uosaki, An efficient electrocatalyst for oxygen reduction to water – boron nitride nanosheets decorated with small gold nanoparticles (~5 nm) of narrow size distribution on gold substrate, *J. Electroanal. Chem.* 819 (2018) 107–113.
- [11] G. Gao, A. Mathkar, E.P. Martins, D.S. Galvão, D. Gao, P.A. da Silva Autreto, C. Sun, L. Cai, P.M. Ajayan, Designing nanoscaled hybrids from atomic layered boron nitride with silver nanoparticle deposition, *J. Mater. Chem. A* 2 (2014) 3148–3154.
- [12] H. Goto, A. Takagaki, R. Kikuchi, S.T. Oyama, Hydrogenation of 2,5-dimethylfuran on hexagonal-boron nitride- and silica-supported platinum catalysts, *Appl. Catal. A* 548 (2017) 122–127.
- [13] C. Huang, Q. Liu, W. Fan, X. Qiu, Boron nitride encapsulated copper nanoparticles: a facile one-step synthesis and their effect on thermal decomposition of ammonium perchlorate, *Sci. Rep.* 5 (2015) 16736.
- [14] D.H. Kim, M. Lee, B. Ye, H.-K. Jang, G.T. Kim, D.-J. Lee, E.-S. Kim, H.D. Kim, Catalytically-etched hexagonal boron nitride flakes and their surface activity, *Appl. Surf. Sci.* 402 (2017) 254–260.
- [15] D. Fan, X. Lv, J. Feng, S. Zhang, J. Bai, R. Lu, J. Liu, Cobalt nickel nanoparticles encapsulated within hexagonal boron nitride as stable, catalytic dehydrogenation nanoreactor, *Int. J. Hydrogen Energy* 42 (2017) 11312–11320.
- [16] R. Nie, R. Sang, X. Ma, Y. Zheng, X. Cheng, W. Li, L. Guo, H. Jin, Y. Wu, Copper-γ-cyclodextrin complexes immobilized on hexagonal boron nitride as an efficient catalyst in the multicomponent synthesis of 1,2,3-triazoles, *J. Catal.* 344 (2016) 286–292.
- [17] A. Harley-Trochimczyk, T. Pham, J. Chang, E. Chen, M.A. Worsley, A. Zettl, W. Mickelson, R. Maboudian, Platinum nanoparticle loading of boron nitride aerogel and its use as a novel material for low-power catalytic gas sensing, *Adv. Funct. Mater.* 26 (2016) 433–439.
- [18] Y.A. Krutyakov, A.A. Kudrinskiy, A.Y. Olenin, G.V. Lisichkin, Synthesis and properties of silver nanoparticles: advances and prospects, *Russ. Chem. Rev.* 77 (2008) 233–257.
- [19] N.L. Pacioni, C.D. Borsarelli, V. Rey, A.V. Veglia, Synthetic routes for the preparation of silver nanoparticles, in: E. Alarcon, M. Griffith, K. Udekwu (Eds.), *Silver Nanoparticle Applications*, Engineering Materials, Springer, Cham, 2015, https://doi.org/10.1007/978-3-319-11262-6_2.
- [20] K. Shameli, M.B. Ahmad, S.D. Jazayeri, S. Sedaghat, P. Shabanzadeh, H. Jahangirian, M. Mahdavi, Y. Abdollahi, Synthesis and characterization of polyethylene glycol mediated silver nanoparticles by the green method, *Int. J. Mol. Sci.* 13 (2012) 6639–6650.
- [21] M.B. Ahmad, M.Y. Tay, K. Shameli, M.Z. Hussein, J.J. Lim, Green synthesis and characterization of silver/chitosan/polyethylene glycol nanocomposites without any reducing agent, *Int. J. Mol. Sci.* 12 (2011) 4872–4884.
- [22] S. Nishimura, D. Mott, A. Takagaki, S. Maenosono, K. Ebitani, Role of base in the formation of silver nanoparticles synthesized using sodium acrylate as a dual reducing and encapsulating agent, *Phys. Chem. Chem. Phys.* 13 (2011) 9335–9343.
- [23] N. Fleitas-Salazar, E. Silva-Campa, S. Pedrosa-Santana, J. Tanori, M.R. Pedroza-Montero, R. Riera, Effect of temperature on the synthesis of silver

- nanoparticles with polyethylene glycol: new insights into the reduction mechanism, *J. Nanoparticle Res.* 19 (2017) 113.
- [24] Z. Shervani, Y. Ikushima, M. Sato, H. Kawanami, Y. Hakuta, T. Yokoyama, T. Nagase, H. Kuneida, K. Aramaki, Morphology and size-controlled synthesis of silver nanoparticles in aqueous surfactant polymer solutions, *Colloid Polym. Sci.* 286 (2008) 403–410.
- [25] S.H. Im, Y.T. Lee, B. Wiley, Y. Xia, Large-scale synthesis of silver nanocubes: the role of HCl in promoting cube perfection and monodispersity, *Angew. Chemie – Int. Ed.* 44 (2005) 2154–2157.
- [26] Y.M. Dai, T.C. Pan, W.J. Liu, J.M. Jehng, Highly dispersed Ag nanoparticles on modified carbon nanotubes for low-temperature CO oxidation, *Appl. Catal. B Environ.* 103 (2011) 221–225.
- [27] S. Mozghan, S. Talebi, I. Kazeminezhad, M. Nematpour, Synthesis and characterization of Ag@Carbon core-shell spheres as a novel catalyst for room temperature N-arylation reaction, *J. Catal.* 361 (2018) 339–346.
- [28] J. Xu, W. Yang, H. Chen, L. Zheng, M. Hu, Y. Li, X. Fang, Efficiency enhancement of TiO₂ self-powered UV photodetectors using a transparent Ag nanowire electrode, *J. Mater. Chem. C* 6 (2018) 3334–3340.
- [29] R.J. Chimentão, I. Kirm, F. Medina, X. Rodríguez, Y. Cesteros, P. Salagre, J.E. Sueiras, Different morphologies of silver nanoparticles as catalysts for the selective oxidation of styrene in the gas phase, *Chem. Commun. (Camb)* 7 (2004) 846–847.
- [30] S. Coskun, B. Aksoy, H.E. Unalan, Polyol synthesis of silver nanowires: an extensive parametric study, *Cryst. Growth Des.* 11 (2011) 4963–4969.
- [31] C. Ducamp-Sanguesa, R. Herrera-Urbina, M. Figlarz, Synthesis and characterization of fine and monodisperse silver particles of uniform shape, *J. Solid State Chem.* 100 (1992) 272–280.
- [32] H. Wang, X. Qiao, J. Chen, X. Wang, S. Ding, Mechanisms of PVP in the preparation of silver nanoparticles, *Mater. Chem. Phys.* 94 (2005) 449–453.
- [33] S. Nam, D.V. Parikh, B.D. Condon, Q. Zhao, M. Yoshioka-Tarver, Importance of poly(ethylene glycol) conformation for the synthesis of silver nanoparticles in aqueous solution, *J. Nanoparticle Res.* 13 (2011) 3755–3764.
- [34] J.A. Adekoya, E.O. Dare, M.A. Mesubi, A.A. Nejo, H.C. Swart, N. Revaprasadu, Synthesis of polyol based Ag/Pd nanocomposites for applications in catalysis, *Results Phys.* 4 (2014) 12–19.
- [35] Y. Krutyakov, P. Zhrebina, A. Kudrinskiy, Y. Zubavichus, M. Presniakov, A. Yapyntsev, A. Karabtseva, D. Mikhaylov, G. Lisichkin, New frontiers in water purification: highly stable amphopolycarboxylate-stabilized Ag–AgCl nanocomposite and its newly discovered potential, *J. Phys. D: Appl. Phys.* 49 (2016) 375501.
- [36] Ç. Güldür, F. Balıkcı, Catalytic oxidation of CO over Ag-Co/alumina catalysts, *Chem. Eng. Commun.* 190 (2003) 986–998.
- [37] V.V. Dutov, G.V. Mamontov, V.I. Zaikovskii, L.F. Liotta, O.V. Vodyankina, Low-temperature CO oxidation over Ag/SiO₂ catalysts: effect of OH/Ag ratio, *Appl. Catal. B Environ.* 221 (2018) 598–609.
- [38] X. Zhang, Z. Qua, X. Lia, M. Wena, X. Quana, D. Mab, J. Wu, Studies of silver species for low-temperature CO oxidation on Ag/SiO₂ catalysts, *Sep. Purif. Technol.* 72 (2010) 395–400.
- [39] D. Widmann, A. Krautsieder, P. Walter, A. Brückner, R.J. Behm, How temperature affects the mechanism of CO oxidation on Au/TiO₂: a combined EPR and TAP reactor study of the reactive removal of TiO₂ surface lattice oxygen in Au/TiO₂ by CO, *ACS Catal.* 6 (2016) 5005–5011.
- [40] M. Sun, Q. Fu, L. Gao, Y. Zheng, Y. Li, M. Chen, X. Bao, Catalysis under shell: improved CO oxidation reaction confined in Pt@h-BN core-shell nanoreactors, *Nano Res.* 10 (2017) 1403–1412.
- [41] T.M. Tran-Thuy, C.C. Chen, S.D. Lin, Spectroscopic studies of how moisture enhances CO oxidation over Au/BN at ambient temperature, *ACS Catal.* 7 (2017) 4304–4312.
- [42] F. Müller, S. Grandthyll, Monolayer formation of hexagonal boron nitride on Ag (001), *Surf. Sci.* 617 (2013) 207–210.
- [43] A. Konopatsky, K. Firestein, D. Leybo, Z. Popov, K. Larionov, A. Steinman, A. Matveev, A. Manakhov, A. Kovalskii, P. Sorokin, D. Golberg, D. Shtansky, BN nanoparticle/Ag hybrids with enhanced catalytic activity: theory and experiments, *Catal. Sci. Technol.* 8 (2016) 1652–1662.
- [44] K. Firestein, D. Kvashnin, A. Sheveyko, I. Sukhorukova, A. Kovalskii, A. Matveev, O. Lebedev, P. Sorokin, D. Golberg, D. Shtansky, Structural analysis and atomic simulation of Ag/BN nanoparticle hybrids obtained by Ag ion implantation, *Mater. Des.* 98 (2016) 167–173.
- [45] K. Firestein, D. Leybo, A. Steinman, A. Kovalskii, A. Matveev, A. Manakhov, I. Sukhorukova, P. Slukin, N. Fursova, S. Ignatov, D. Golberg, D. Shtansky, BN/Ag hybrid nanomaterials with petal-like surfaces as catalysts and antibacterial agents, *Beilstein J. Nanotechnol.* 9 (2018) 250–261.
- [46] Z. Lu, P. Lv, Z. Yang, S. Li, D. Ma, R. Wu, A promising single atom catalyst for CO oxidation: Ag on boron vacancies of h-BN sheets, *Phys. Chem. Chem. Phys.* 19 (2017) 16795–16805.
- [47] X. Wang, Z. Yan, H. Zhou, X. Zhang, J. Jia, H. Wu, O₂ activation and CO oxidation on n-p codoped h-BN single-atom catalysts, *Comput. Theor. Chem.* 1127 (2018) 31–36.
- [48] Y. Zhang, L. Xu, B. Tang, Z. Li, Controllable synthesis, property investigation of hexagonal boron nitride micromesh and its functionalization by Ag nanoparticles, *Catal. Sci. Technol.* 3 (2013) 222–229.
- [49] A.K. Rajagopal, J. Callaway, Inhomogeneous electron gas, *Phys. Rev. B* 7 (1973) 1912–1919.
- [50] W. Kohn, L.J. Sham, Self-consistent equations including exchange and correlation effects, *Phys. Rev.* 140 (1965) 1133–1138.
- [51] P.E. Blöchl, Projector augmented-wave method, *Phys. Rev. B* 50 (1994) 17953–17979.
- [52] D. Joubert, From ultrasoft pseudopotentials to the projector augmented-wave method, *Phys. Rev. B – Condens. Matter Mater. Phys.* 59 (1999) 1758–1775.
- [53] G. Kresse, J. Hafner, Ab initio molecular dynamics for liquid metals, *Phys. Rev. B* 47 (1993) 558–561.
- [54] G. Kresse, J. Hafner, Ab initio molecular-dynamics simulation of the liquid-metal–amorphous-semiconductor transition in germanium, *Phys. Rev. B* 49 (1994) 14251–14269.
- [55] G. Kresse, J. Furthmüller, Efficient iterative schemes for ab initio total-energy calculations using a plane-wave basis set, *Phys. Rev. B – Condens. Matter Mater. Phys.* 54 (1996) 11169–11186.
- [56] J.P. Perdew, K. Burke, M. Ernzerhof, Generalized gradient approximation made simple, *Phys. Rev. Lett.* 77 (1996) 3865–3868.
- [57] G. Henkelman, H. Jónsson, Improved tangent estimate in the nudged elastic band method for finding minimum energy paths and saddle points, *J. Chem. Phys.* 113 (2000) 9978–9985.
- [58] J.D. Pack, H.J. Monkhorst, “Special points for Brillouin-zone integrations” – a reply, *Phys. Rev. B* 16 (1977) 1748–1749.
- [59] S. Grimme, Semiempirical GGA-type density functional constructed with a long-range dispersion correction, *J. Comput. Chem.* 27 (2006) 1787–1799.
- [60] K. Momma, F. Izumi, VESTA 3 for three-dimensional visualization of crystal, volumetric and morphology data, *J. Appl. Crystallogr.* 44 (2011) 1272–1276.
- [61] M. Marcos, D. Cabaleiro, M. Guimarey, M. Comuñas, L. Fedele, J. Fernández, L. Lugo, PEG 400-Based phase change materials nano-enhanced with functionalized graphene nanoplatelets, *Nanomaterials* 8 (2017) 16.
- [62] I.M. Deygen, E.V. Kudryashova, New versatile approach for analysis of PEG content in conjugates and complexes with biomacromolecules based on FTIR spectroscopy, *Colloids Surf B Biointerfaces* 141 (2016) 36–43.
- [63] N. Mendoza, F. Paraguay-Delgado, L. Hechavarría, M.E. Nicho, H. Hu, Nanostructured polyethylene glycol-titanium oxide composites as solvent-free viscous electrolytes for electrochromic devices, *Sol. Energy Mater. Sol. Cells* 95 (2011) 2478–2484.
- [64] B. Sharma, A. Mahata, S. Mandani, T.K. Sarma, B. Pathak, Coordination polymer hydrogels through Ag(I)-mediated spontaneous self-assembly of unsubstituted nucleobases and their antimicrobial activity, *RSC Adv.* 6 (2016) 62968–62973.
- [65] M. Xue, Y. Lü, Q. Sun, K. Liu, Z. Liu, P. Sun, Ag(I)-Coordinated supramolecular metallogels based on schiff base ligands: structural characterization and reversible thixotropic property, *Cryst. Growth Des.* 15 (2015) 5360–5367.
- [66] Y. Zhou, J.M. Perket, J. Zhou, Growth of Pt nanoparticles on reducible CeO₂(111) thin films: effect of nanostructures and redox properties of Ceria, *J. Phys. Chem. C* 114 (2010) 11853–11860.
- [67] P. Luches, F. Pagliuca, S. Valeri, F. Illas, G. Preda, G. Pacchioni, Nature of Ag islands and nanoparticles on the CeO₂(111) surface, *J. Phys. Chem. C* 116 (2012) 1122–1132.
- [68] E. Marzbánrad, G. Rivers, P. Peng, B. Zhaoac, N.Y. Zhou, How morphology and surface crystal texture affect thermal stability of a metallic nanoparticle: the case of silver nanobelts and pentagonal silver nanowires, *Phys. Chem. Chem. Phys.* 17 (2015) 315–324.
- [69] C. Stampfl, M. Scheffler, Density-functional theory study of the catalytic oxidation of CO over transition metal surfaces, *Surf. Sci.* 433 (1999) 119–126.
- [70] C.M. Chang, C. Cheng, C.M. Wei, CO oxidation on unsupported Au₅₅, Ag₅₅, and Au₂₅Ag₃₀ nanoclusters, *J. Chem. Phys.* 128 (2008) 124710.